Title

Analysis of time-dependent strain heterogeneity in shales using X-ray microscopy and digital volume correlation

Authors

Rassouli, Fatemeh S
Lisabeth, Harrison

Publication Date

2021-08-01

DOI

10.1016/j.jngse.2021.103984

Peer reviewed

ANALYSIS OF TIME-DEPENDENT STRAIN HETEROGENEITY IN SHALES USING X-RAY MICROSCOPY AND DIGITAL VOLUME CORRELATION

Fatemeh S. RASSOULI*:
Department of Geophysics, Stanford University.
397 Panama Mall, B59, Stanford, CA 94305
+1-408-502-0066
frasouli@stanford.edu

Harrison LISABETH
Earth and Environmental Science Area, Lawrence Berkeley National Laboratory
1 Cyclotron Rd, Berkeley, CA 94720
hlisabeth@lbl.gov

Abstract: In this paper, we report the results of a 4-dimensional (3 spatial dimensions plus time) in-situ creep experiment on a milli-core shale plug from Barnett formation in Texas. An outstanding challenge in shale mechanics is connecting observable characteristics to predictable mechanical and hydraulic behavior. We employ novel imaging and analysis techniques to statistically link sample mineralogy and structure to observed deformation. In particular, we focus on mechanisms of porosity reduction during transient response to step changes in stress, analogous to the aseismic deformation that occurs after an episode of fracturing. An uniaxial creep experiment was conducted inside an Xradia Versa 520 micro-CT system for 12 hours at room temperature under a constant uniaxial stress of 25 MPa. A Digital Volume Correlation (DVC) method was employed to measure micro-scale deformation of the sample by comparing the resulting volumetric images with a high-resolution scan of the sample obtained prior to the creep experiment. The results indicate that the time-dependent deformation in the compliant clay plus kerogen matrix constituents facilitates rigid grain rotation and compaction of intergranular porosity at the boundary between rigid grains and matrix.

Keywords: Shale, Time-dependent deformation, X-ray microscopy, Digital Volume Correlation (DVC)

1. Introduction

Hydraulic fracturing technology combined with horizontal drilling has made it feasible to produce oil and gas from low-permeability, unconventional reservoirs over the past few decades. Deriving an understanding the behavior of these unconventional oil and gas reservoirs based on fundamental mechanical, hydraulic and mineralogical characteristics is critically important to optimize production (King et al., 2010; Yao, 2012). However, characterization of shale using traditional methods and models has proven difficult. Shale is extremely fine-grained, anisotropic and heterogeneous. Small-scale analysis tends to overlook heterogeneity while large-scale analysis cannot resolve micro- and nano-scale processes that have proven essential to understanding the petrophysics of shale. In this paper, we present and discuss the application of new rock mechanics testing, imaging and image analysis techniques to link mineralogy to mechanical behavior using a workflow that could be automated to increase sample throughput, allowing high resolution analysis to be applied at larger scales.

Mineralogy has been shown to have the greatest impact on ductility of shale rocks (Sone and Zoback, 2014b; Rassouli and Zoback, 2018). Shales with higher amount of ductile clay minerals and organic matter tend to behave more viscoplastically (Beaudoin et al., 2011; King et al., 2010; Kundert et al., 2009; Skomedal, 2016; Sone and Zoback, 2014b; Yao, 2012). The vertical propagation of hydraulic fractures is controlled by variations of the magnitude of the least principal stress with depth (Hubbert and Willis, 1972), which appear to be controlled by relative degrees of viscoplastic relaxation of stress (Sone and Zoback, 2014; Zoback and Kohli, 2019). Viscoplastic relaxation in rocks reduces the difference between the maximum and minimum horizontal stresses and creates a more isotropic state of stress. Fractures initiated in ductile formations close, which reduces permeability (Nygard et al., 2006), while fractures initiated in brittle zones tend to result in permeability increase. Developing quantitative links between a priori observables such as mineralogy and reservoir mechanical response would allow for the design of less risky and more efficient hydrofracture plans.

Simple descriptions of mineralogy may not be sufficient to describe shales, however, as structural complexity, heterogeneity and presence of nano-scale pores (Nelson, 2009; Kuila and Prasad, 2012) challenge traditional notions connecting rock physics with reservoir geomechanics. There is a great interest in quantifying the heterogeneous distribution of strain in various materials (Etxegarai et al., 2017; Hall et al., 2009; Paz-Garcia et al., 2016; Viggiani et al., 2004). In traditional laboratory mechanics testing, the distribution of the strain is treated as homogeneous on the sample scale, an assumption that breaks down when looking in detail at clay-rich rocks. The challenge then becomes how to quantify a rock that is both heterogeneous and nano-scale.

X-ray tomography is a tool commonly used to address heterogeneity in rock samples. Many studies on porous rocks like sandstones (e.g. Alshibli and Alramahi, 2006; And_o et al., 2013;

Katagiri et al., 2010), coarse grain carbonates (e.g. Baud et al., 2017; Cilona et al., 2014) or heterogeneous argillaceous rocks (Lenoir et al., 2007) have been conducted to understand the mechanical behavior of these rocks under uniaxial and triaxial loading using x-ray images from before and after or, more recently, during experiments. In some studies, grain-scale kinematics of sandstone (e.g. Ando et al., 2013), pressure solution of coarse grain carbonates (e.g. Baud et al., 2017; Cilona et al., 2012), or localized fracture density of damaged samples (e.g. Cilona et al., 2014) have been investigated. All of the above in-situ mechanical experiments were conducted using medical or industrial X-ray CT machines, synchrotrons and neutron diffraction beam setups (e.g. Birmpilis et al., 2017; Covey-Crump et al., 2006; Lenoir et al., 2007).

Metal pressure vessels cannot be used for the in-situ experiments inside traditional X-ray CT machines due to high attenuation (Etxegarai et al., 2017). As a result, only vessels made of epoxy (e.g. Hall et al., 2009) can be used inside these systems, which can limit the amount of applied pressure to the sample and image resolution. Using neutron imaging circumvents this problem, as most metal alloys have little interaction with neutrons; therefore, high-pressure triaxial experiments can be conducted inside these systems. The drawbacks of using neutron techniques are a lower signal to noise ratio, lower resolution at the same pixel size and complexities using the system (Covey-Crump et al., 2006; Tudisco et al., 2015). Synchrotrons can give high-resolution images in very short periods of time, making the method appealing especially for experiments involving fast fracture evolutions compared to industrial X-ray CT machines, however these systems have very limited accessibility compared to industrial X-ray CT sources (Tudisco et al., 2015). One may ask, how can we better employ technology to increase the efficiency of these experiments?

We can leverage advances in computational image analysis methods to increase the through-put of in-situ deformation experiments so we can explore micro-scale processes in high resolution while studying enough small-scale samples to effectively upscale results. Small-scale heterogeneous structure can be measured from the images acquired from the methods discussed above using adaptive thresholding and Digital Volume Correlation (DVC) methods can be used to map deformation in 3-Dimensions (3D). The combination of these two methods can yield powerful results.

In this study, we describe and discuss an in-situ creep experiment on a mini-core of clay-rich shale from Barnett formation. The experiment was conducted at room temperature using a compressional/extensional loading stage inside an X-ray computed tomography microscope under a constant applied 25 MPa uniaxial stress. The resulting 3D projection images from the first hour of the experiment were then compared to those acquired at the end of the experiment to measure heterogeneous time-depended deformations and compared to mineralogy.

2. Experiments

2.1. Sample Description

The sample we used in this study was from Barnett formation (Newark East field), Fort Worth Basin in Texas, a shallow, north-south-elongated basin associated with the late Paleozoic Ouachita orogeny (Montgomery et. al., 2005). This field was recognized as the largest producing gas field in Texas in 2006 (EIA, 2006). The primary producing facies of the Barnett is volumetrically composed of mainly quartz and clay and less calcite minerals (Bowker, 2007). Production from Barnett is more challenging than other formations because of its greater depths of production and resulting higher pressures, its complex and multiphase thermal history and thermogenic origin (Montgomery et. al., 2005).

The sample we used here contained 22.9 wt% clay, 8.9 wt% calcite, 55 wt% quartz and 6.15 wt% TOC. We used a diamond impregnated drill with an inner diameter of 4.5 mm to drill a milli-core from a vertical core plug. To avoid swelling and damage of clay minerals, we used oil-based fluid as drilling lubricant and applied high-pressure air while drilling to help the extraction of cuttings from the outer surface of the drilling bit. We used a twist drill bit holder to hold the specimens while grinding and polishing its bases with sandpaper to make the ends parallel.

2.2. Experimental Procedure

In this study we used a Zeiss Xradia Versa 520 X-ray microscope (XRM), which is equipped with a load-cell rig chain capable of rotating the loading stage for image acquisition purposes. A Deben CT5000 5kN compression/extension stage was used to apply an axial load to the samples, which was measured with a load cell with a resolution of 25mN mounted at the upper part of the chamber. Load was applied by a screw-driven actuator motor located at the bottom part of the loading stage. A MICROTEST tensile stage control software was used to control the applied load and temperature. The middle part of the Deben cell is hollow with loading platens at the top and bottom and is surrounded by a glassy carbon wall, which is transparent to the X-ray as shown Figure 1. The loading stage was equipped with cooling tubes to allow water flow around the chamber to control the inner temperature of the XRM. We scanned the sample with a 4.78-micron voxel size resolution prior to the in-situ creep experiment to provide a detailed 3D view of the sample for further image analysis and segmentation (Table 1).

We used glassy carbon plates above and below the sample as spacers to make a gap between the steel loading platens and the top and bottom of the sample. The μ-CT images of these plates create marker lines for further image analysis.

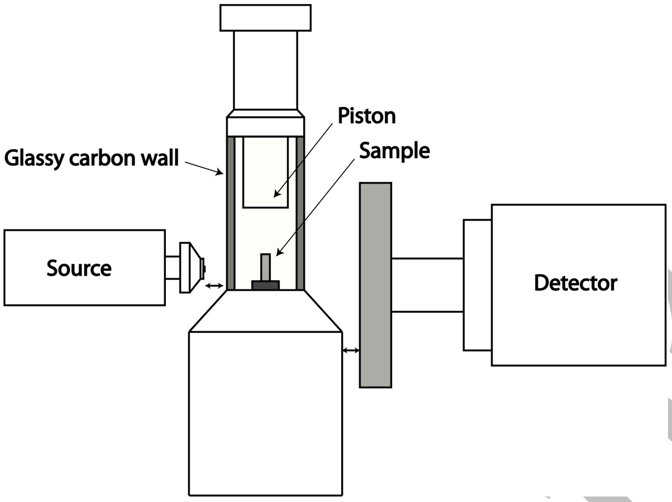

Figure 1: Schematic of the loading system and position of source and detector with respect to the loading stage. The two-headed arrows show the limitation of the source/detector travel distances.

We attached these spacers to the loading platens using weak fluorescent glue. Additionally, we applied a very small amount of the same glue around the lower perimeter of the specimens to fix its position and avoid shifting problems while capturing the X-ray tomographs. The glue used for this purpose was weak enough to not change the boundary conditions of the experiment significantly.

We conducted the creep test at room temperature in a dry and drained condition. Load was increased with a rate of 80 N/min to a constant value of 400 N (~ 25 MPa) and was kept at this level for the entire experimental time. After reaching the constant load, a complete scan of the sample was obtained by taking 1024 radiographs at different equal angles covering a range of 180° of the stage rotation during every hour of the experiments. The radiographic slices were orthogonal to the axis of rotation of the specimens during the scans.

The resolution of these scans was decreased to 14-micron voxel size because of the travel distance limitation of both the source and the detector as a result of the glassy carbon wall presence (Figure 1). The objective magnification was 0.4X for all the scans. The source energies for the in-situ experiments and the high-resolution scans were 90 and 60 kV, respectively. The specifications of the instrument settings are listed in Table 1.

Resolution	Duration (Hours)	Source Distance (mm)	Detector Distance (mm)	Exposure Time (Sec)	Projection Number
4.87 (High resolution)	2	21.99	8.47	1.5	1010
13.9 (In-situ test)	12	62.00	240.00	2	1024

Table 1. μCT instrument setting for each of scans

3. Image Analysis

We used a commercial Objective Research System (ORS) visualization and analysis software to process the images from the high-resolution scans for adaptive thresholding analysis. Additionally, we used the same software to crop out the surrounding in addition to the two ends of the sample and picked the exact same inner volume in the two sets of images (from the first and last hour of the experiment) for the DVC analysis. These inner volumes are cut in a cubical shape to avoid end and edge effects and to obtain a volume of the sample with more uniform attenuation numbers.

We followed the procedure that is reported in detail in Rassouli et al., 2017 to segment the 3D reconstruction of the high-resolution images by composition. In this procedure we selected component thresholds based upon the shape of the CT-number histogram and verified the results in 2D using SEM images (Figure 2).

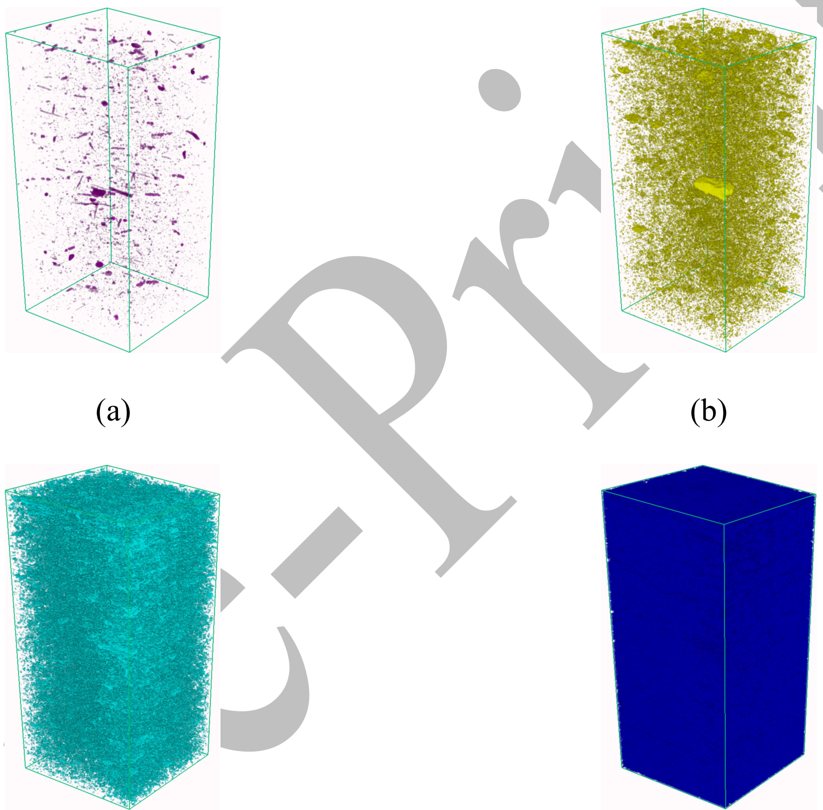

(a) (b)

(c) (d)

(e) (f)

Figure 2. Mineral segmentation of the Barnett sample; (a) pyrite (b) apatite, (c) carbonates, (d) matrix (e) organic matter and (f) porosity.

We collected the SEM images in addition to elemental maps on an FEI Magellan 400 XHR with a Bruker Quantax XFlash 6160 Energy Dispersive Spectroscopy (EDS). To collect and analyze the EDS data, we used Quantax Esprit 2.1 software. The phases identified are pyrite, apatite, carbonates, matrix, organic matter and porosity. The carbonate group consists of both calcite and dolomite. The matrix group consists of very fine-grained silicates, largely clay, but including quartz and feldspar as well.

To measure the deformation of the sample we employed the code TomoWarp2 (Tudisco et al., 2017), an open source DVC technique that works by first defining nodes, equally spaced within the reference image. Correlation windows are then delimited, in which the nodes are centrally located. The node spacing and correlation window size can be adjusted to optimize the resolution of the result. The correlation coefficient for each displacement of the correlation window within a search window is then calculated. The maximum correlation is found and used to compute the discrete displacement of each node. Using user defined sample dimensions, the discrete displacement field is then used to calculate the full strain tensor.

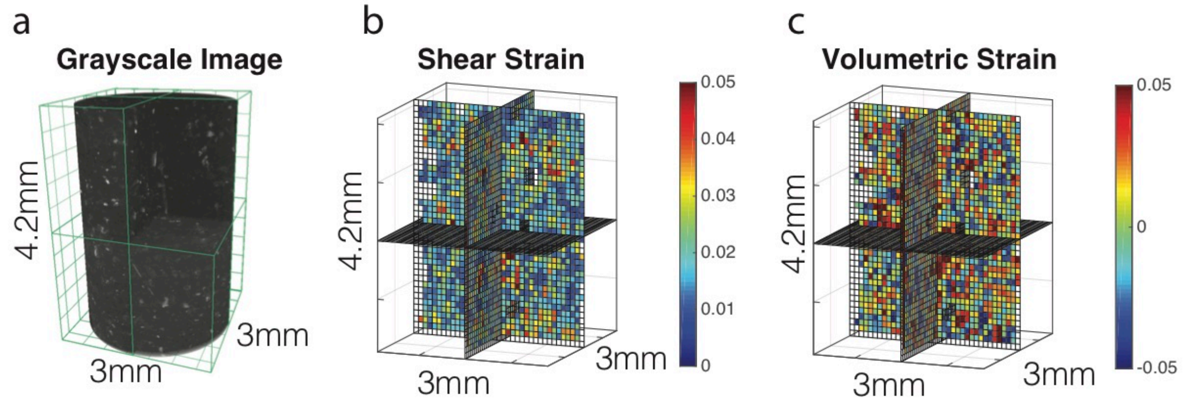

Figure 3. Results from DVC code. a) Greyscale tomography data. Lighter minerals are large carbonate and phosphate grains, darker minerals are fine-grained matrix. b) Volumetric strain, negative strain indicates dilatancy. c) Shear strain, positive strain indicates right lateral displacement.

4. Results

An example of the results from the DVC code are presented in Figure 3b-c, showing that deformation was dominated by shearing and slightly compactive. The average bulk shear strain was 2% and ranged from 0 to 5% in some places. The average bulk volumetric strain is 0.3% but ranged from very slight dilation (<1%) to moderate compaction (~4%). Areas of dilation appear to correspond with regions of contrasting material properties such as where a rigid carbonate or phosphate grains are suspended in a clay and organic matrix. This is possibly due to rigid rotation producing new intergranular pore space.

Using the mineralogically thresholded CT data and strain field from DVC, we can quantitatively link microscale deformation to mineralogical heterogeneity. The thresholded CT data is in the form of binary 3D arrays for each phase and the DVC data is two 3D arrays of strain values, shear and volumetric. Average values are calculated from each circular cross-sectional slice of the sample cylinder to reduce these arrays to a series of profiles representing the volume fraction of each phase in the case of the mineralogically thresholded data, and average strain in the case of the DVC data (Figure 4). The mineralogical volume fraction profiles are akin to a micro-scale mineralogy log from a well. These profiles are then registered using the top of the sample and the higher-resolution data down sampled to ensure the profiles have the same number of slices. The ultimate resolution of the line averages is ~100 microns per slice. The registered and resampled data is then normalized by removing the mean and dividing by the standard deviation along each individual profile. The normalized data is then cross-correlated, producing Pearson's Correlation Coefficient (R) and concomitant statistical p-value.

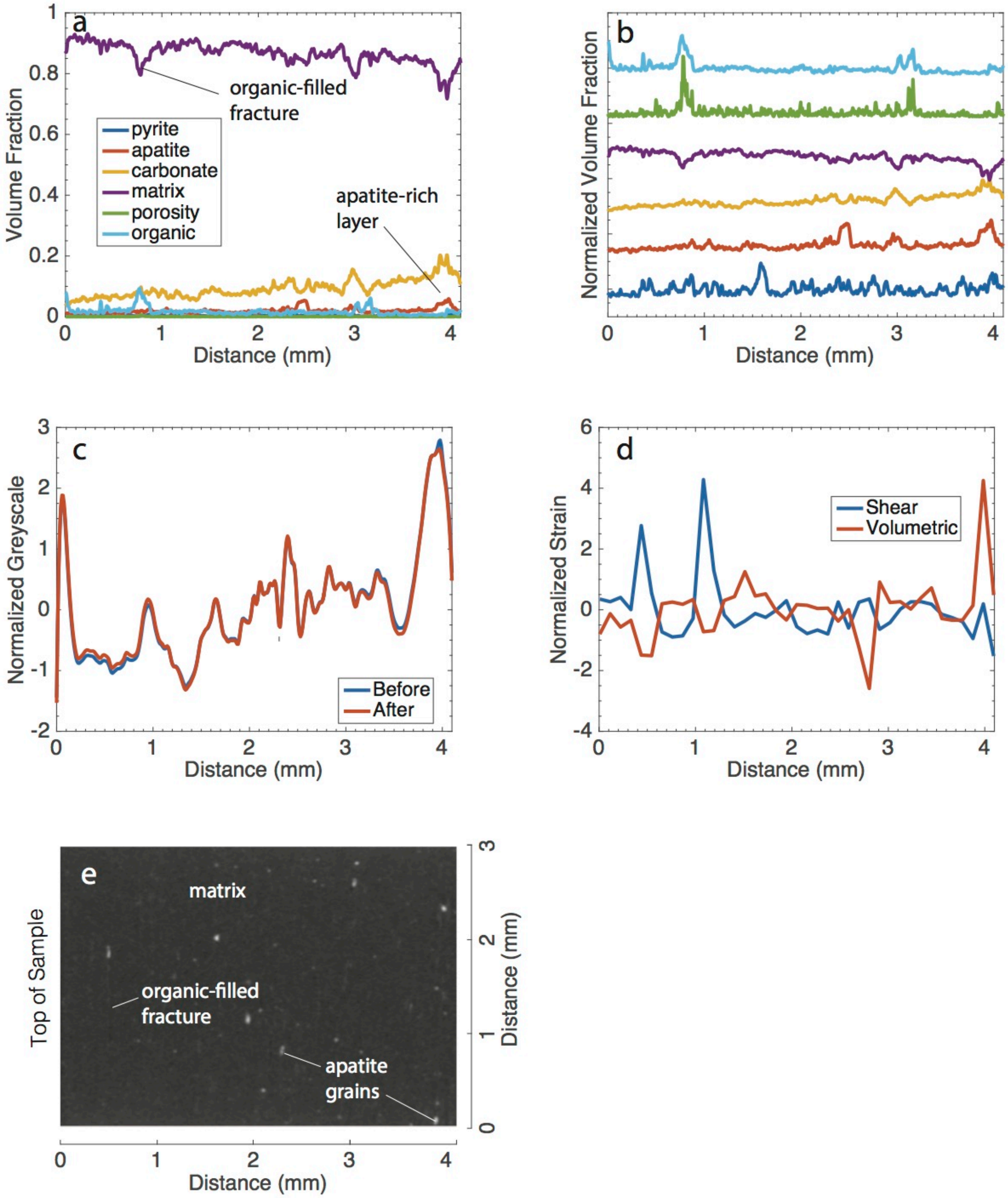

Figure 4. Line averages from Mineralogical, CT and DVC data. Distances are measured from the top of the sample. a) Volume fraction of threshold mineral phases. d) Normalized volume fractions used in cross correlation analysis. Coloring is the same as panel (a). c) Normalized greyscale of before and after CT images. In slightly higher average values indicate

reduction of porosity over the course of the deformation. d) Normalized strain from the DVC algorithm. Both volumetric and shear strain show periodic behavior and are in general anticorrelated. e) Slice through the center of the tomography data taken before compaction. Some structural and mineralogical features are annotated.

The results of the cross-correlations are listed in Table 2. The correlation coefficient, R, can be interpreted as the fraction of particular type deformation that can be linearly related to the presence of a given phase and the concomitant p-value can be interpreted as the likelihood that this correlation could be the result of random chance. Using the standard p-value threshold of 0.05, we can begin to make associations in the data.

The strongest correlation with volumetric strain is CT number, which roughly corresponds to density. The mineralogically thresholded data confirms this with statistically significant positive correlations between compaction and apatite and carbonate phases and negative correlations between compaction and matrix. The strongest correlation with shear strain is with the matrix. CT number has a statistically significant negative correlation with shear strain as well, which is also consistent with shear strain predominantly partitioning into less dense matrix minerals. Minor phases such as pyrite, porosity and organics do not exhibit significant correlations.

	Volumetric		Shear	
	R	p	R	p
CT number	0.4953	0.0013	-0.3865	0.0151

Porosity	-0.1127	0.4946	0.1011	0.5404
Pyrite	-0.0331	0.8417	-0.0636	0.7005
Carbonate	0.3681	0.0211	-0.2918	0.0714
Matrix	-0.3895	0.0142	0.4221	0.0074
Apatite	0.4032	0.0109	-0.4261	0.0068
Organics	-0.1026	0.5343	0.0111	0.9463

Table 2. Results from DVC. R-values are Pearson's Correlation Coefficient, a value from -1 to 1 indicating degree of correlation and or anticorrelation. The p-values are the statistical likelihood that the correlation could be the result of random variation.

5. Discussion

The bulk mechanical behavior of our sample is consistent with previously published data on Barnett shale samples at similar conditions. Sone and Zoback 2014a, report a creep compliance of 0.5x10^{-5} for a Barnett sample with less than 10 wt% carbonate, 40 wt% clay and 50 wt% QFP at 45 MPa axial stress. This yields a volumetric strain of 0.2%, which is comparably to our bulk volumetric strain result of 0.3%. Sone suggests that the majority of this deformation is accommodated by compaction of porosity in the clay and organics. Our results confirm that substantial deformation occurs in the compliant matrix, but this deformation is primarily shear and is generally anticorrelated with volumetric deformation (i.e. compaction). This suggests that the low strength and friction of clay minerals facilitate shear sliding and grain rearrangement.

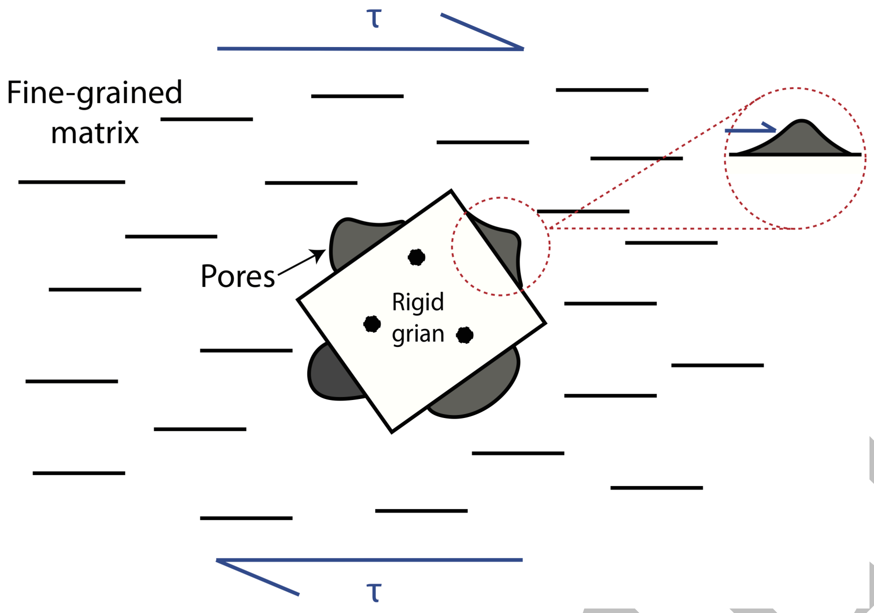

Figure 5. Conceptual model for matrix response to stress perturbations due to hydraulic stimulation. Changes in the stress field around new tensile fractures lead to shear deformation of compliant clay minerals, which facilitates the closure of intergranular porosity at the margins of rigid grains. This reduces bulk porosity, shutting down flow paths and reducing permeability and productivity in a time-dependent manner.

Fracture networks control reservoir permeability to first order. Low porosity reservoirs with few fractures have characteristically low permeabilities, which is why hydraulic fracturing has become the standard treatment for such reservoirs. However, the declining productivity of stimulated reservoirs post-stimulation remains a challenge. In addition to the creation of new fractures, hydraulic stimulation perturbs the stress state of a reservoir, resulting in creep. The deformation associated with this creep can be very small, yet still have a substantial impact on flow within the reservoirs. In order for oil and gas to be produced from a fracture network, the fluids must migrate from the matrix into the fracture, flowing through a tight network of small pores, possibly dominated by the larger pores, which exist at the boundaries of rigid grains. Our results indicate that creep due to stress perturbation manifests as shear in the compliant matrix, enhancing compaction of these important pores. A conceptual representation is presented in Figure 5.

This model is supported by a closer look at the microstructures of the Barnett shale. Though micro- and nano-pores exist in the clay matrix of the rock, it is unclear to what extent these pores are interconnected and contribute a permeably network. The meso- and macro-pores, in conjunction with natural and induced fracture networks, are likely to be the primary control on flow paths. SEM images of a Barnett sample from the same depth as the sample used in our experiment are presented in Figure 6. Examination of these images shows that substantial meso- and macro-porosity exists at the boundaries of apatite and carbonate grains. This is a feature that commonly exists in clay-rich shales [e.g. Sondergeld et al., 2010]. These pores, between 20 and 100 microns in diameter, are too small to be represented individually by our DVC results due the down sampling necessary to find representative volumes for successful correlation; however, the code can identify sub-voxel deformations. Therefore, these pores are grouped in with the rigid clasts during segmentation, which is why an association is found between those grains and volumetric deformation. It appears shear deformation of compliant matrix results in the compaction of large pores along the boundaries of rigid grains. This may have implications for how creep affects permeability and production in the Barnett shale.

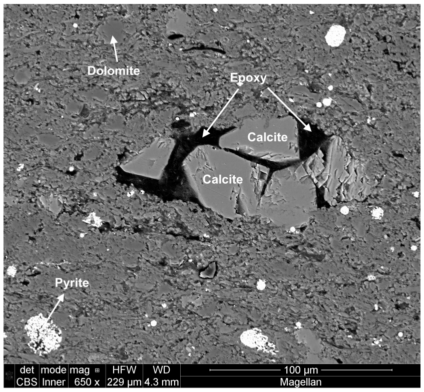
Dolomite
Epoxy
Calcite
Calcite
Pyrite
det mode mag HFW WD 100 µm
CBS Inner 650 x 229 µm 4.3 mm Magellan

(a)

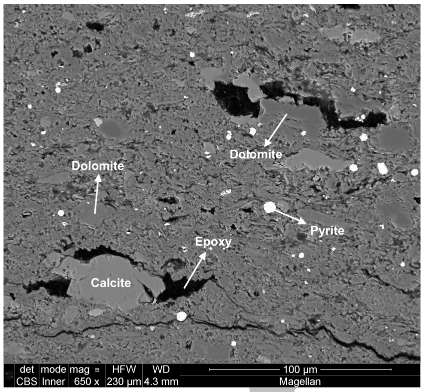
Dolomite
Dolomite
Pyrite
Epoxy
Calcite
det mode mag HFW WD 100 µm
CBS Inner 650 x 230 µm 4.3 mm Magellan

(b)

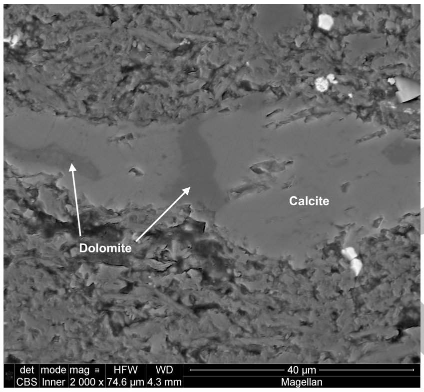
Calcite
Dolomite
det mode mag HFW WD 40 µm
CBS Inner 2 000 x 74.6 µm 4.3 mm Magellan

(c)

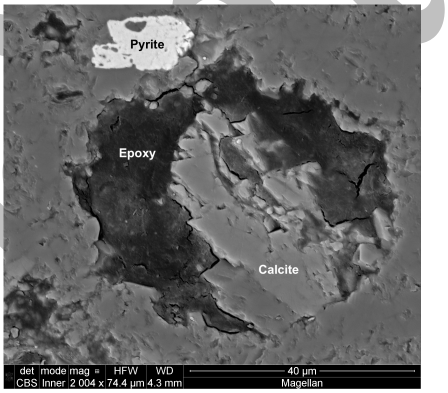
Pyrite
Epoxy
Calcite
det mode mag HFW WD 40 µm
CBS Inner 2 004 x 74.4 µm 4.3 mm Magellan

(d)

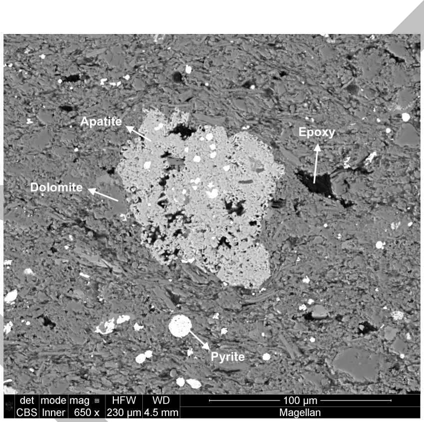
Apatite
Epoxy
Dolomite
Pyrite
det mode mag HFW WD 100 µm
CBS Inner 650 x 230 µm 4.5 mm Magellan

(e)

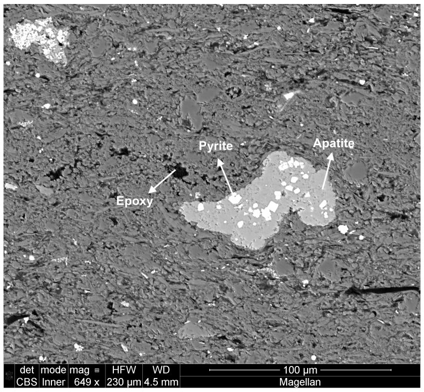
Pyrite
Apatite
Epoxy
det mode mag HFW WD 100 µm
CBS Inner 649 x 230 µm 4.5 mm Magellan

(f)

Figure 6. SEM images of experimental sample show typical fabrics. Large (~100 micron), rigid carbonate and apatite grains suspended in fine-grained (>5 micron) matrix. Substantial intergranular porosity is evident around the fringes of large rigid grains suspended in fine-grained matrix. a) cluster of calcite grains with interstitial porosity, b) calcite grain showing partial dolomitization with substantial intergranular porosity, c) close-up view of dolomite replacement texture in a large calcite grain, d) calcite grain fringed with a large pore., e) apatite grain with wormy porosity, f) pyrite grains intergrown with large apatite.

6. Conclusions

We performed in-situ creep tests on Barnett shale in an x-ray microscope in order to assess the extent and sources of deformation heterogeneity in clay-rich rocks. We used a novel adaptive thresholding algorithm to identify the mineralogical structure of the rock and coupled it with Digital Volume Correlation in order to quantitatively link strain and mineralogy. We find:

(1) Shear deformation is associated with clay minerals and volumetric deformation is associated with apatite and carbonate minerals. This confirms that shear deformation in the compliant matrix facilitates rigid grain rotation and compaction of intergranular porosity at the boundary between grains and matrix.

(2) Our workflow leverages several new hardware as well as software technologies and offers the possibility of the high throughput testing necessary to characterize the heterogeneous behavior of shale rocks. This can lead to acceleration of understanding through automation of the process.

Acknowledgment

References

Alshibli, K.A., and Alramahi, B.A., 2006, Microscopic evaluation of strain distribution in granular materials during shear: Journal of geotechnical and geo-environmental engineering, v. 132, no. 1, p. 80-91.

Andò, E., Viggiani, G., Hall, S., and Desrues, J., 2013, Experimental micro-mechanics of granular media studied by x-ray tomography: recent results and challenges: Geotechnique Letters, v. 3, no. 3, p. 142-146.

Baud, P., Hall, S., Ji, Y., Wong, T.F., and Heap, M.J., 2017, The brittle-ductile transition in porouslimestone imaged by x-ray computed tomography and digital image correlation, in Poromechanicsvi: p. 1782-1788.

Beaudoin, W.P., Khalid, S., Allison, J., Faurschou, K., et al., 2011, Horn river basin: A study of the behavior of frac barriers in a thick shale package using the integration of microseismic, geomechanics and log analysis, in Canadian unconventional resources conference: Society of Petroleum Engineers.

Birmpilis, G., Dijkstra, J., Tudisco, E., and Hall, S., 2017, In-situ study of deformation mechanisms of soft clay using x-ray computed tomography and digital volumetric correlation: Proceedings ICTMS2017.

Bowker, K.A., 2007. Barnett shale gas production, Fort Worth Basin: Issues and discussion. AAPG bulletin, 91(4), pp.523-533.

Cilona, A., Baud, P., Tondi, E., Agosta, F., Vinciguerra, S., Rustichelli, A., and Spiers, C.J., 2012,Deformation bands in porous carbonate grainstones: field and laboratory observations: Journal of Structural Geology, v. 45, p. 137-157.

Cilona, A., Faulkner, D.R., Tondi, E., Agosta, F., Mancini, L., Rustichelli, A., Baud, P., and Vinciguerra,S., 2014, The effects of rock heterogeneity on compaction localization in porous carbonates: Journal of Structural Geology, v. 67, p. 75-93.

Covey-Crump, S.J., Holloway, R.F., Scho_eld, P.F., and Daymond, M.R., 2006, A new apparatus for measuring mechanical properties at moderate confining pressures in a neutron beamline: Journal of applied crystallography, v. 39, no. 2, p. 222-229.

DOE, U., EIA, 2006. Manufacturing Energy Consumption Survey (MECS)-2006 Data, EIA, Washington, DC.

Etxegarai, M., Tudisco, E., Tengattini, A., Hall, S., and Viggiani, G., 2017, Hydromechanical behavior of porous rock studied with neutron tomography: Proceedings ICTMS2017.

Hall, S., Lenoir, N., Viggiani, G., Desrues, J., and Bésuelle, P., 2009, Strain localization in sand under triaxial loading: characterization by x-ray micro tomography and 3d digital image correlation, in Proceedings of the 1st international symposium on computational geomechanics (comgeo i), juan-lespins, cote d'azur, france, april: .

Hubbert, M.K., and Willis, D.G., 1972, Mechanics of hydraulic fracturing: .

Katagiri, J., Matsushima, T., and Yamada, Y., 2010, Simple shear simulation of 3d irregularly-shaped particles by image-based dem: Granular Matter, v. 12, no. 5, p. 491-497.

King, G.E., Haile, L., Shuss, J.A., Dobkins, T., et al., 2008, Increasing fracture path complexity and controlling downward fracture growth in the Barnett shale, in SPE shale gas production conference: Society of Petroleum Engineers.

King, G.E., et al., 2010, Thirty years of gas shale fracturing: What have we learned?, in SPE annual technical conference and exhibition: Society of Petroleum Engineers.

Kulia, U., Prasad, M., Derkowski, A. and McCarty, D.K., 2012. Compositional controls on mudrock pore-size distribution: an example from Niobrara Formation: Society of Petroleum Engineers Annual Technical Conference and Exhibition. San Antonio, Texas, USA.

Kundert, D.P., Mullen, M.J., et al., 2009, Proper evaluation of shale gas reservoirs leads to a more effective hydraulic-fracture stimulation, in SPE rocky mountain petroleum technology conference: Society of Petroleum Engineers.

Lenoir, N., Bornert, M., Desrues, J., Bésuelle, P., and Viggiani, G., 2007, Volumetric digital image correlation applied to x-ray microtomography images from triaxial compression tests on argillaceous rock: Strain, v. 43, no. 3, p. 193-205.

Montgomery, S.L., Jarvie, D.M., Bowker, K.A. and Pollastro, R.M., 2005. Mississippian Barnett Shale, Fort Worth basin, north-central Texas: Gas-shale play with multi–trillion cubic foot potential. AAPG bulletin, 89(2), pp.155-175.

Nygård, R., Gutierrez, M., Bratli, R.K., and Høeg, K., 2006, Brittle-ductile transition, shear failure and leakage in shales and mudrocks: Marine and Petroleum Geology, v. 23, no. 2, p. 201-212.

Nelson, S.G. and Huff, C.D., 2009, January. Horizontal Woodford Shale Completion Cementing Practices in the Arkoma Basin, Southeast Oklahoma: A Case History. In SPE Production and Operations Symposium. Society of Petroleum Engineers.

Paz-Garcia, J., Taiwo, O., Tudisco, E., Finegan, D., Shearing, P., Brett, D., and Hall, S., 2016, 4danalysis of the microstructural evolution of si-based electrodes during lithiation: Time-lapse x-ray imaging and digital volume correlation: Journal of Power Sources, v. 320, p. 196-203.

Quintanilla-Terminel, A., Zimmerman, M.E., Evans, B. and Kohlstedt, D.L., 2017. Microscale and nanoscale strain mapping techniques applied to creep of rocks. *Solid Earth*, *8*(4).

Rassouli, F. S., Ross, C. M., Zoback, M. D., Andrew, M., 2017. Shale Rock Characterization Using Multi-Scale Imaging. 51st American Rock Mechanics Association, San Francisco, CA, USA

Skomedal, Ø., 2016, Formation of a shale barrier using numerical and analytical methods [Master's thesis]: NTNU.

Sondergeld, C.H., Ambrose, R.J., Rai, C.S. and Moncrieff, J., 2010, January. Micro-structural studies of gas shales. In SPE unconventional gas conference. Society of Petroleum Engineers.

Sone, H., and Zoback, M.D., 2014a, Time-dependent deformation of shale gas reservoir rocks and its long-term effect on the in situ state of stress: International Journal of Rock Mechanics and Mining Sciences, v. 69, p. 120-132.

Sone, H., and Zoback, M.D., 2014b, Viscous relaxation model for predicting least principal stress magnitudes in sedimentary rocks: Journal of Petroleum Science and Engineering, v. 124, p. 416-431.

Tudisco, E., Hall, S., Charalampidou, E.M., Kardjilov, N., Hilger, A., and Sone, H., 2015, Full-field measurements of strain localization in sandstone by neutron tomography and 3d-volumetric digital image correlation: Physics Procedia, v. 69, p. 509-515.

Viggiani, G., Lenoir, N., Besuelle, P., Di Michiel, M., Marello, S., Desrues, J., and Kretzschmer, M.,2004, X-ray microtomography for studying localized deformation in _ne-grained geomaterials under triaxial compression: Comptes rendus Mecanique, v. 332, no. 10, p. 819-826.

Yao, Y., 2012, Linear elastic and cohesive fracture analysis to model hydraulic fracture in brittle and ductile rocks: Rock mechanics and rock engineering, v. 45, no. 3, p. 375-387.

Zoback, M.D., 2010, Reservoir geomechanics: Cambridge University Press.